

Influence of ^{14}N hyperfine interaction on electron nuclear double resonance of boron vacancy in hexagonal boron nitride

G.V. Mamin^{1,*}, E.V. Dmitrieva¹, F.F. Murzakhanov¹, I.N. Gracheva¹, V.A. Soltamov²,
M.R. Gafurov¹

¹Institute of Physics, Kazan Federal University, Kremlyovskaya 18, Kazan 420008, Russia

²Ioffe Institute, Polytekhnicheskaya, 26, St.Petersburg 194021, Russia

*E-mail: george.mamin@kpfu.ru

(Received ????? ??, ????, revised ?????, ????,
accepted ?????, ????, published ?????, ????)

The research focuses on the explanation of a phenomenon observed in the spectra of electron-nuclear resonance (ENDOR) pertaining to nitrogen atoms adjacent to the boron vacancy (V_{B}^-) defect in hexagonal boron nitride (hBN). The phenomenon is manifested as a shift of the ENDOR spectrum lines with respect to the nitrogen Larmor frequency. It is hypothesized that these shifts are indicative of a substantial hyperfine interaction between the V_{B}^- defect and the ^{14}N nuclei in hBN. A calculation utilizing second-order perturbation theory was executed to determine the positions of the ENDOR spectrum lines, resulting in the formulation of correction equations. The values obtained from the perturbation theory corrections align well with the experimental results. The extent of nuclear state admixture into electron states was found to be around 0.04–0.07%.

PACS: 71.70.-d, 71.70.Jp, 75.10.Dg, 76.30.-v, 76.70.Dx, 76.30.Mi, 73.90.+f

Keywords: ESR, ENDOR, boron vacancy, hBN

1. Introduction

Presently, there is an ongoing exploration of quantum technology systems capable of functioning without sophisticated and expansive cryogenic facilities (at temperatures $T > 4.2$ K) while accommodating a scalable number of qubits. The most recognized spin qubits include the nitrogen-vacancy (NV^-) center in diamond [1] and various spin centers found in silicon carbide (SiC) [2]. However, the potential for utilizing electron qubits in conjunction with nuclear spin systems is constrained to a single nitrogen nucleus unless costly isotopic enrichment with nuclei possessing a magnetic moment is employed. In contrast, hexagonal boron nitride (hBN) features nuclei (^{14}N , ^{11}B , ^{10}B) that are each associated with an electron center at a boron vacancy (V_{B}^-), all of which possess a magnetic moment (See Figures 1 A, B). This characteristic may significantly enhance the application of standard CNOT-type operations by leveraging different types of nuclei, thereby facilitating the integration of hBN into quantum computing frameworks [3]. Furthermore, hBN is classified as a two-dimensional (2D) material [4], which enables the utilization of paramagnetic centers situated near the surface, particularly through the combination of microwave and optical radiation, presenting opportunities for advanced ultrasensitive nanosensors [5]. In contrast, in three-dimensional (3D) materials, the proximity of spin centers to the surface tends to degrade their spin coherence time [6]. Additionally, the integration of hBN with other 2D materials has the potential to markedly enhance the sensitivity of these systems to various external influences.

In previous publications from our research group, we demonstrated the efficacy of high-field electron-nuclear double resonance (ENDOR) for both qualitative and quantitative analyses of electron-nuclear interactions in (nano)diamonds [7] and SiC [8]. Our investigation into ENDOR has now been broadened to include hexagonal boron nitride (hBN). Through this extension, we

have identified several novel features that had not been observed in earlier studies. This paper aims to elucidate these findings and provide potential explanations for the observed phenomena.

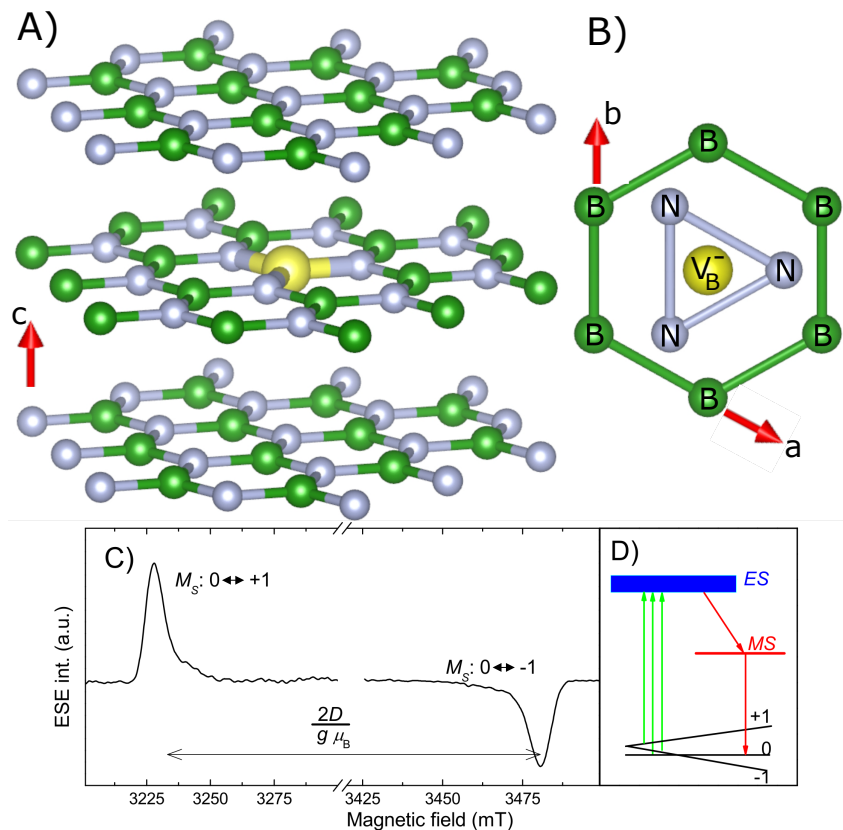


Figure 1. A), B) Schematic presentation of hBN lattice with V_B^- defect. For B) the c -axis is oriented perpendicular to the plane of the figure. C) ESR spectrum of the defects at the temperature of 50 K under 532 nm excitation and $\mathbf{B}_0 \parallel c$. Splitting between fine structure transitions is represented by $\frac{2D}{g\mu_B}$, with D signifying zero field splitting. Fine structure components corresponding to the ESR transition with selection rules $\Delta M_S = 1$ within the $S = 1$ manifold are indicated as $0 \leftrightarrow +1$ and $0 \leftrightarrow -1$. D) Scheme of the $M_S = 0$ spin initialization by 532 nm excitation.

2. Materials

The hBN single crystals with dimensions of $900 \mu\text{m} \times 540 \mu\text{m} \times 55 \mu\text{m}$ used in this study were commercially produced by the HQ Graphene company. The samples were irradiated at room temperature with 2 MeV electrons to a total dose $6 \times 10^{18} \text{ cm}^{-2}$. No annealing treatments were applied to the irradiated samples.

3. Methods

The electron spin resonance (ESR) experiments were carried out on the W-band (operating at the microwave (MW) frequency of 94 GHz) Bruker Elexsys E680 commercial spectrometer (Karlsruhe, Germany) can be deleted. The ESR spectra in a pulsed mode were registered by detecting the amplitude of the primary electron spin echo (ESE) as a function of the magnetic field sweep B_0 using a pulse sequence $\frac{1}{2}\pi(\text{MW})-\tau-\pi(\text{MW})-\tau-\text{ESE}$, where $\pi(\text{MW}) = 80 \text{ ns}$ and $\tau = 240 \text{ ns}$. ENDOR spectra were obtained utilizing the Mims pulse sequence

$\frac{1}{2}\pi(\text{MW})-\tau-\frac{1}{2}\pi(\text{MW})-t_1-\pi(\text{RF})-t_2-\frac{1}{2}\pi(\text{MW})-\tau$ -ESE with a 150 W radiofrequency (RF) generator, where $\pi(\text{RF}) = 160 \mu\text{s}$. Low temperature ($T=50 \text{ K}$) measurements were conducted by using a flow helium cryostat from Oxford Instruments. The sample's photoexcitation was provided by green laser ($\lambda = 532 \text{ nm}$) with an output power of 200 mW.

4. Results and Discussion

ESR spectrum of the V_B^- defects in hBN sample under continuous optical excitation and orientation of \mathbf{B}_0 parallel to the hexagonal c axis is presented in Figure 1 C along with the scheme of the spin initialization with the light (Figure 1 D, where ES stands for the excited state, MS is for the metastable state, see reference [4]).

For $\mathbf{B}_0 \parallel c$ the ESR spectrum can be described by the following spin-Hamiltonian

$$\hat{\mathbf{H}} = g\mu_B B_0 S_z + D \left(S_z^2 - \frac{S(S+1)}{3} \right) + \sum_{j=1}^3 \left(A_{zz} S_z I_{z(i)} - A_{xx} S_x I_{x(i)} + A_{yy} S_y I_{y(i)} - \gamma \hbar B_0 I_z + P \left(3I_{z(i)}^2 - I(I+1) \right) \right), \quad (1)$$

where the first two terms determine electronic structure of the spin defect with the g -factor $g = -2.004$ and the zero-field splitting (ZFS) constant $D = 3.55 \text{ GHz}$. The next three terms describe the anisotropic hyperfine interaction (with components A_{xx} , A_{yy} , A_{zz}) of the electron magnetic moment with the ^{14}N nucleus and the last term is nuclear quadrupole interaction (NQI) $P = \frac{1}{h} \frac{e^2 Q q}{4I(2I-1)} = \frac{1}{h} \frac{e^2 Q q}{4}$, where i is the index of the nitrogen nucleus from the three nearest atoms of the immediate environment (Figure 1) [9]. In previous papers [10] the $C_q = \frac{e^2 Q q}{h} = 4P$ value has been used. The electron S and nuclear I spins are equal 1. The interaction between the nuclei is neglected.

The experimental ESR spectrum shown in Figure 1 C demonstrates a pair of ESR transitions that serve as fingerprints of the ZFS structure associated with the $S = 1$ for the V_B^- defect, manifesting itself by the splitting in magnetic field by the value $2D$, where $D = 3.55 \text{ GHz}$ is the zero field splitting of the V_B^- defect, and $\frac{g\mu_B}{h} = 28 \text{ GHz/T}$ is its gyromagnetic ratio. An important feature of the spectrum is that the fine structure components are inverted in phase relative to each other, mimicking a significant deviation of triplet spin sublevels population from Boltzmann statistics due to optical excitation and indicating population inversion, as shown in the scheme presented in Figure 1 D. For the purpose of calculating ENDOR spectra, we take into account only one of the three identical ^{14}N nuclear spins. In this alignment of the magnetic field relative to the c -axis, the hyperfine coupling has previously been established to be $A_{xx} \approx 45.5 \text{ MHz}$ [1, 11]. The last two terms in equation 3 refer to the interaction of the ^{14}N nuclear magnetic moment with the static external magnetic field and the interaction of ^{14}N nuclear electric quadrupole moment with the electric field gradient produced by the surrounding atoms. The nuclear quadrupole constant, which characterizes the the corresponding splitting through nuclear quadrupole interaction (NQI) has been determined to be $C_q \approx 2.11 \pm 0.08 \text{ MHz}$ [11]. To account for the bond direction [10], in the Hamiltonian in crystals coordinates, S_z must be replaced by S_x and S_x by S_z , excluding Zeeman interaction. All three nitrogen nuclei are equivalent for $\mathbf{B}_0 \parallel c$ axis, and the summation over these nuclei can be removed. Also, we take into account the closeness of values of A_{xx} and A_{yy} [10, 11], and to facilitate the calculations, we replace A_{yy} by A_{xx} . Creating new variables: $Z_e \equiv g\mu_B B_0$, $Z_n \equiv \gamma \hbar B_0$, one can rewrite eq. 1 as

$$\hat{\mathbf{H}} = Z_e + D \left(S_z^2 - \frac{S(S+1)}{3} \right) + A_{xx} S_z I_z - A_{zz} S_x I_x + A_{xx} S_y I_y - Z_n + P (3I_x^2 - I(I+1)). \quad (2)$$

In general, to analyse the ESR spectra, it is sufficient to consider the energy values obtained while neglecting the off-diagonal elements in the spin-Hamiltonian matrix, and these values are presented in equation 3. The corresponding energy level diagram is also shown in Figure 2 with ENDOR transitions indicated by arrows.

$$\begin{aligned} E_1^{(0)} &= -Z_e + \frac{D}{3} + A_{xx} + Z_n - \frac{3}{2}P, \\ E_2^{(0)} &= -Z_e + \frac{D}{3} + P, \\ E_3^{(0)} &= -Z_e + \frac{D}{3} - A_{xx} - Z_n - \frac{3}{2}P, \\ E_4^{(0)} &= -\frac{2D}{3} + Z_n - \frac{3}{2}P, \\ E_5^{(0)} &= -\frac{2D}{3} + P, \\ E_6^{(0)} &= -\frac{2D}{3} - Z_n - \frac{3}{2}P, \\ E_7^{(0)} &= Z_e + \frac{D}{3} - A_{xx} + Z_n - \frac{3}{2}P, \\ E_8^{(0)} &= Z_e + \frac{D}{3} + P, \\ E_9^{(0)} &= Z_e + \frac{D}{3} + A_{xx} - Z_n - \frac{3}{2}P, \end{aligned} \quad (3)$$

Thus, the following transitions should be observed in the ENDOR spectrum:

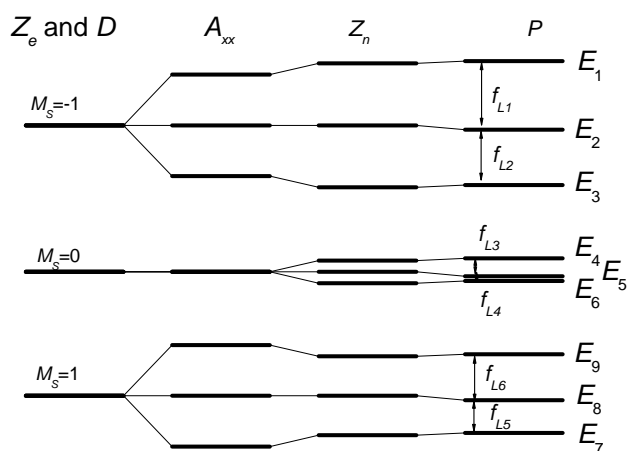


Figure 2. Schematic diagram of energy levels of the $\text{V}_\text{B}\text{-N}_3$ defect.

$$\begin{aligned}
 f_{L1}^{(0)} &= A_{xx} + Z_n + \frac{3}{2}P, \\
 f_{L2}^{(0)} &= A_{xx} + Z_n - \frac{3}{2}P, \\
 f_{L3}^{(0)} &= Z_n + \frac{3}{2}P, \\
 f_{L4}^{(0)} &= Z_n - \frac{3}{2}P, \\
 f_{L5}^{(0)} &= A_{xx} - Z_n - \frac{3}{2}P, \\
 f_{L6}^{(0)} &= A_{xx} - Z_n + \frac{3}{2}P,
 \end{aligned} \tag{4}$$

where the lower index Li corresponds to ENDOR transition on Figure 2. According to equation 4, one can identify two groups of symmetrical lines (pairs) that have to appear in the ENDOR spectrum. The first set, comprising lines $L3$ and $L4$, is found in proximity to the nuclear Zeeman value (Z_n), and the second quadrupole pair ($L1, L2$ or $L5, L6$) is positioned near the $A_{xx} \pm Z_n$ values. The separation between the pairs within each group is equivalent to $3P$.

The ENDOR spectra were acquired on both fine structure components low field (L): $0 \leftrightarrow +1$ ($B_0(L) = 3223.1$ mT, lower spectrum) and high field (H): $0 \leftrightarrow -1$ ($B_0(H) = 3480.5$ mT, upper spectrum) as shown in Figure 3 A, B for $\mathbf{B}_0 \parallel c$ and $0 \leftrightarrow -1$ ($B_0(L) = 3287.15$ mT, Figure 3 C, D) for $\mathbf{B}_0 \perp c$ axis. For $\mathbf{B}_0 \perp c$, the three nitrogen nuclei become nonequivalent (see Figure 1 B), and, therefore, three spectra with slightly different parameters are observed for each type of nuclei. The corresponding lines are designated by upper indices as ', ", and "''. The calculated Z_n values for both values $B_0(L)$ and $B_0(H)$ are shown in Figures 3 A,C by green vertical lines. As one can clearly see already from Figure 3, the lines in pairs are arranged asymmetrically relative to the Z_n .

To obtain more accurate numerical parameters of the ENDOR spectra, the observed ENDOR lines are fitted by Gaussian curves (red curves in Figure 3). Positions and widths of the resonant nuclear transitions are summarized in Table 1. Additionally, the pair splitting of lines in pair and the value of center of the pair (pair midpoint) added to Table 1 for comparing with NQI splitting and values of Z_n ($B_0(L) = 3223.1$ mT) = 9.9198 MHz, $Z_n(B_0(H) = 3480.5$ mT) = 10.7120 MHz for $\mathbf{B}_0 \parallel c$ and $Z_n(B_0(L) = 3287.1$ mT) = 10.1167 MHz for $B_0 \perp c$. The ENDOR linewidth Δf is used to estimate the error bars in the line position designated as $\frac{\Delta f}{5}$.

The data presented in Table 1 indicates that the midpoint of each pair of lines $L3$ and $L4$ is displaced towards higher frequencies relative to the Larmor frequency, specifically by approximately 0.06 ± 0.01 MHz for $\mathbf{B} \parallel c$ and 0.03 ± 0.01 and 0.09 ± 0.01 MHz respectively, for $\mathbf{B} \perp c$.

Additionally, the corresponding NQI splitting can be determined as $3P = 1.58 \pm 0.01$ MHz (Table 1) or $P = 0.53$ MHz, with the C_q value calculated as $4P = 2.11 \pm 0.01$ MHz for crystall orientation $\mathbf{B} \parallel c$. For $\mathbf{B} \perp c$, the value $3P =$ ranges from 2.58 MHz to 0 consistent with the function $3\cos^2\theta - 1$, where 6° , 54° , and 66° represents the angle between main axis for each nonequivalent type of nitrogen nucleus and magnetic field direction. Note that this study does not consider the non-axiality of the NQI $\eta=0.07$, resulting in increased C_q by factor $(1+\eta) = 1.07$ time compared to reference [10].

In the following analysis, we will explore the effects of the off-diagonal terms of the spin Hamiltonian matrix by applying perturbation theory. The diagonal segment of the spin Hamil-

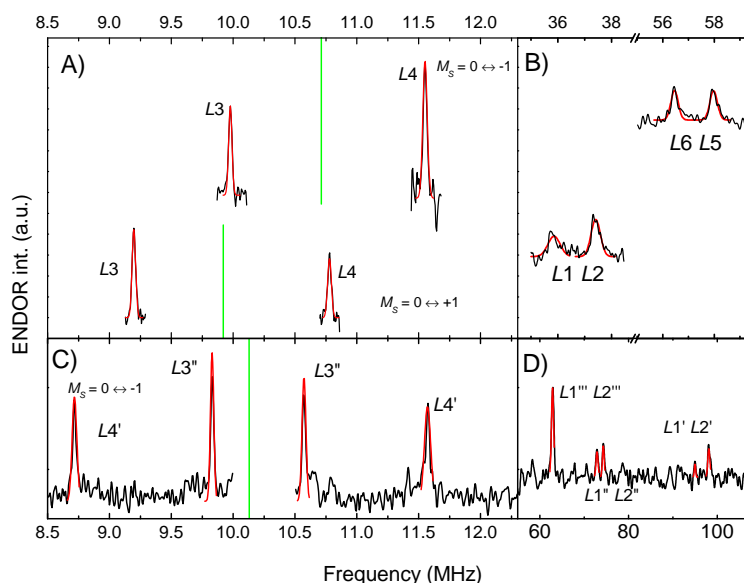


Figure 3. ^{14}N ENDOR spectrum for two electronic transitions with $M_S = 0 \leftrightarrow +1$ ($B_0(L) = 3223.1$ mT, top) and $0 \leftrightarrow -1$ ($B_0(H) = 3480.5$ mT, lower spectrum) recorded at $T = 50$ K. The numbers ($L1-L6$) correspond to the distinct resonance transitions presented in the energy diagram (Figure 2). ^{14}N Larmor frequency in a given magnetic fields is indicated by a green lines. A, B) $\mathbf{B}_0 \parallel c$. C, D) $\mathbf{B}_0 \perp c$.

Table 1. Key parameters of ^{14}N ENDOR line positions. The line splitting corresponds to distance between f_{L3} and f_{L4} , or f_{L1} and f_{L2} , or f_{L5} and f_{L6} frequencies in pairs. Midpoints of pairs are calculated as $\frac{f_{L3}+f_{L4}}{2}$, $\frac{f_{L1}+f_{L2}}{2}$, $\frac{f_{L5}+f_{L6}}{2}$ value

	N	Frequency, MHz	Splitting of lines in pair, MHz	Midpoint of pair, MHz
$B_0(L) = 3223.1$ mT, $B_0 \parallel c$	L3	9.198 ± 0.005	1.58 ± 0.01	9.99 ± 0.01
	L4	10.778 ± 0.005		
	L1	35.9 ± 0.2	1.6 ± 0.3	36.65 ± 0.3
	L2	37.4 ± 0.2		
$B_0(H) = 3480.5$ mT, $B_0 \parallel c$	L3	9.977 ± 0.005	1.58 ± 0.01	10.76 ± 0.01
	L4	11.552 ± 0.005		
	L5	56.5 ± 0.1	1.5 ± 0.2	57.25 ± 0.2
	L6	58.0 ± 0.1		
$B_0(L) = 3287.15$ mT, $B_0 \perp c$	L3'	8.718 ± 0.005	2.85 ± 0.01	10.144 ± 0.01
	L4'	11.571 ± 0.005		
	L3''	9.83 ± 0.005	0.7428 ± 0.01	10.201 ± 0.01
	L4''	10.5728 ± 0.005		

tonian matrix, as outlined in equation 3, will be employed as the initial approximation. As a perturbation operator, we take the lagging off-diagonal part of the spin Hamiltonian matrix:

$$\hat{\mathbf{V}} = \begin{bmatrix} 0 & 0 & \frac{3P}{2} & 0 & -a_{zpx} & 0 & 0 & 0 & 0 \\ 0 & 0 & 0 & -a_{zmx} & 0 & -a_{zpx} & 0 & 0 & 0 \\ \frac{3P}{2} & 0 & 0 & 0 & -a_{zmx} & 0 & 0 & 0 & 0 \\ 0 & -a_{zmx} & 0 & 0 & 0 & \frac{3P}{2} & 0 & -a_{zpx} & 0 \\ -a_{zpx} & 0 & -a_{zmx} & 0 & 0 & 0 & -a_{zmx} & 0 & -a_{zpx} \\ 0 & -a_{zpx} & 0 & \frac{3P}{2} & 0 & 0 & 0 & -a_{zmx} & 0 \\ 0 & 0 & 0 & 0 & -a_{zmx} & 0 & 0 & 0 & \frac{3P}{2} \\ 0 & 0 & 0 & -a_{zpx} & 0 & -a_{zmx} & 0 & 0 & 0 \\ 0 & 0 & 0 & 0 & -a_{zpx} & 0 & \frac{3P}{2} & 0 & 0 \end{bmatrix}, \quad (5)$$

where $a_{zmx} \equiv \frac{A_{zz}-A_{xx}}{2}$, $a_{zpx} \equiv \frac{A_{zz}+A_{xx}}{2}$. The wave functions enumerated as

$|M_S = -1, M_I = -1\rangle$, $|M_S = -1, M_I = 0\rangle$, $|M_S = -1, M_I = 1\rangle$, $|M_S = 0, M_I = -1\rangle$, ..., $|M_S = 1, M_I = 1\rangle$.

In the first order of perturbation theory for the operator $\hat{\mathbf{V}}$, the corrections to the energy values are equal to zero but the wave functions change as

$$\begin{aligned} \Psi_1 &\approx |M_S = -1, M_I = -1\rangle + \frac{3P}{4A_{xx}} |M_S = -1, M_I = 1\rangle + \frac{a_{zpx}}{Z_e} |M_S = 0, M_I = 0\rangle, \\ \Psi_2 &\approx |M_S = -1, M_I = 0\rangle + \frac{a_{zmx}}{Z_e} |M_S = 0, M_I = -1\rangle + \frac{a_{zpx}}{Z_e} |M_S = 0, M_I = 1\rangle, \\ \Psi_3 &\approx |M_S = -1, M_I = 1\rangle - \frac{3P}{4A_{xx}} |M_S = -1, M_I = -1\rangle + \frac{zmx}{Z_e} |M_S = 0, M_I = 0\rangle, \\ \Psi_4 &\approx |M_S = 0, M_I = -1\rangle + \frac{3P}{4Z_n} |M_S = 0, M_I = 1\rangle - \frac{a_{zmx}}{Z_e} |M_S = -1, M_I = 0\rangle + \\ &+ \frac{a_{zpx}}{Z_e} |M_S = 0, M_I = 0\rangle, \\ \Psi_5 &\approx |M_S = 0, M_I = 0\rangle - \frac{a_{zpx}}{Z_e} |M_S = -1, M_I = -1\rangle - \frac{a_{zmx}}{Z_e} |M_S = -1, M_I = 1\rangle + \\ &+ \frac{a_{zmx}}{Z_e} |M_S = 0, M_I = -1\rangle + \frac{a_{zpx}}{Z_e} |M_S = 0, M_I = 1\rangle, \\ \Psi_6 &\approx |M_S = 0, M_I = 1\rangle - \frac{3P}{4Z_n} |M_S = 0, M_I = -1\rangle - \frac{a_{zpx}}{Z_e} |M_S = -1, M_I = 0\rangle + \\ &+ \frac{a_{zmx}}{Z_e} |M_S = 0, M_I = 0\rangle, \\ \Psi_7 &\approx |M_S = 0, M_I = -1\rangle - \frac{3P}{4A_{xx}} |M_S = 0, M_I = 1\rangle - \frac{a_{zmx}}{Z_e} |M_S = 0, M_I = 0\rangle, \\ \Psi_8 &\approx |M_S = 0, M_I = 0\rangle - \frac{a_{zpx}}{Z_e} |M_S = 0, M_I = -1\rangle - \frac{a_{zmx}}{Z_e} |M_S = 0, M_I = 1\rangle, \\ \Psi_9 &\approx |M_S = 0, M_I = 1\rangle + \frac{3P}{4A_{xx}} |M_S = 0, M_I = -1\rangle - \frac{a_{zpx}}{Z_e} |M_S = 0, M_I = 0\rangle, \end{aligned} \quad (6)$$

where only the largest variables are left in the denominators. As seen, it results in the mixing the wave functions inside the nuclear triplet with good efficiency $\frac{3P}{4Z_n} \approx 7\%$, $\frac{3P}{4A_{xx}} \approx 0.9\%$, and the hyperfine interaction mixes the electron levels with less efficiency $\frac{a_{zmx}}{Z_e} \approx 0.04\%$ or $\frac{a_{zpx}}{Z_e} \approx 0.07\%$.

The energy levels in the second order of perturbation theory can be calculated as

$$E_i^{(2)} = E_i^{(0)} + \sum_j \frac{\langle \Psi_i | \hat{\mathbf{H}} | \Psi_j \rangle^2}{E_i^{(0)} - E_j^{(0)}} \quad (7)$$

Utilizing the values of $E_i^{(0)}$ obtained from equation 3 allows us to express the equation 7 as follows

$$\begin{aligned}
 E_1^{(2)} &= E_1^{(1)} - \frac{a_{zpx}^2}{Z_e} + \frac{9P^2}{8A_{zz}}, \\
 E_2^{(2)} &= E_2^{(1)} + \frac{a_{zmx}^2}{Z_e} - \frac{a_{zpx}^2}{Z_e}, \\
 E_3^{(2)} &= E_3^{(1)} - \frac{a_{zmx}^2}{Z_e} - \frac{9P^2}{8A_{zz}}, \\
 E_4^{(2)} &= E_4^{(1)} + \frac{a_{zmx}^2 - a_{zpx}^2}{Z_e} + \frac{9P^2}{8Z_n}, \\
 E_5^{(2)} &= E_5^{(1)}, \\
 E_6^{(2)} &= E_6^{(1)} - \frac{a_{zmx}^2 - a_{zpx}^2}{Z_e} - \frac{9P^2}{8Z_n}, \\
 E_7^{(2)} &= E_7^{(1)} + \frac{a_{zmx}^2}{Z_e} - \frac{9P^2}{8A_{zz}}, \\
 E_8^{(2)} &= E_8^{(1)} + \frac{a_{zmx}^2}{Z_e} + \frac{a_{zpx}^2}{Z_e}, \\
 E_9^{(2)} &= E_9^{(1)} + \frac{a_{zpx}^2}{Z_e} + \frac{9P^2}{8A_{zz}},
 \end{aligned} \tag{8}$$

where only the largest terms are left in the denominators. Then the positions (RF frequencies) of the ENDOR lines can be expressed as

$$\begin{aligned}
 f_{L1}^{(2)} &= f_{L1}^{(1)} + \frac{(A_{xx} - A_{zz})^2}{4Z_e} + \frac{9P^2}{8A_{zz}}, \\
 f_{L2}^{(2)} &= f_{L2}^{(1)} - \frac{(A_{xx} + A_{zz})^2}{4Z_e} + \frac{9P^2}{8A_{zz}}, \\
 f_{L3}^{(2)} &= f_{L3}^{(1)} - \frac{A_{xx}A_{zz}}{Z_e} + \frac{9P^2}{8Z_n}, \\
 f_{L4}^{(2)} &= f_{L4}^{(1)} - \frac{A_{xx}A_{zz}}{Z_e} + \frac{9P^2}{8Z_n}, \\
 f_{L5}^{(2)} &= f_{L5}^{(1)} + \frac{(A_{xx} + A_{zz})^2}{4Z_e} - \frac{9P^2}{8A_{zz}}, \\
 f_{L6}^{(2)} &= f_{L6}^{(1)} - \frac{(A_{xx} - A_{zz})^2}{4Z_e} - \frac{9P^2}{8A_{zz}}.
 \end{aligned} \tag{9}$$

The theoretical and experimental data merit a comparative analysis. The ENDOR spectra facilitate the numerical determination of parameters such as $\frac{A_{xx}A_{zz}}{Z_e} = -0.04$ MHz, $\frac{9P^2}{8A_{xx}} = 0.004$ MHz, and $\frac{9P^2}{8Z_n} = 0.03$ MHz. Consequently, for $\mathbf{B}_0 \parallel c$, the calculated line shift is $-\frac{A_{xx}A_{zz}}{Z_e} + \frac{9P^2}{8A_{xx}} = 0.07$ MHz, which aligns closely with the experimentally derived value of 0.06 ± 0.01 MHz. For $\mathbf{B}_0 \perp c$, the model forecasts a range of line shifts between $-\frac{(A_{zz}+A_{xx})^2}{9Z_e} - \frac{(2A_{zz}-A_{xx})^2}{9Z_e} = 0.035$ MHz to $-\frac{A_{zz}^2}{Z_e} = 0.08$ MHz. These values are consistent with the experimental data, which spans from 0.03 ± 0.01 and 0.09 ± 0.01 MHz.

5. Summary

In this investigation, we thoroughly explored the effects of the hyperfine interaction between the electron spin and the three nearest nitrogen atoms (^{14}N) on the resulting ENDOR spectra of the boron vacancy defect V_{B}^- in hBN crystal in the W-band. Measurements of the ENDOR spectra for two crystal orientations reveals that this interaction induces a minor but measurable in the W-band shift in the effective nuclear g-factor of ^{14}N , deviating from its established tabulated value. This shift is accompanied by a corresponding change in the ^{14}N Larmor frequency, which we interpret using second-order perturbation theory. Considering the impact of one type of nuclear sublattice on another is essential when developing algorithms for quantum manipulations that involve electronic and nuclear subsystems. This consideration is particularly relevant in the context of enhancing the precision of temperature and magnetic field measurements, such as those conducted by (nano)sensors utilizing boron defects in hBN.

Acknowledgments

Financial support of the Russian Science Foundation under Grant RSF 24-12-00151 is acknowledged.

References

1. Gottscholl A., Kianinia M., Soltamov V., Orlinskii S., Mamin G., Bradac C., Kasper C., Krambrock K., Sperlich A., Toth M., Aharonovich I., Dyakonov V., *Nature Materials* **19**, 540 (2020).
2. Astakhov G., Simin D., Dyakonov V., Yavkin B., Orlinskii S., Proskuryakov I., Anisimov A., Soltamov V., Baranov P., *Applied Magnetic Resonance* **47**, 793 (2016).
3. Cobarrubia A., Schottle N., Suliman D., Gomez-Barron S., Patino C. R., Kiefer B., Behura S. K., *ACS nano* **18**, 22609 (2024).
4. Liu W., Guo N.-J., Yu S., Meng Y., Li Z.-P., Yang Y.-Z., Wang Z.-A., Zeng X.-D., Xie L.-K., Li Q., Wang J.-F., Xu J.-S., Wang Yi-Tao J.-S., Tang, Li C.-F., Guo G.-C. G., *Materials for Quantum Technology* **2**, 032002 (2022).
5. Zhang G., Cheng Y., Chou J.-P., Gali A., *Applied Physics Reviews* **7** (2020).
6. Zhang W., Zhang J., Wang J., Feng F., Lin S., Lou L., Zhu W., Wang G., *Physical Review B* **96**, 235443 (2017).
7. Yavkin B., Gafurov M., Volodin M., Mamin G., Orlinskii S. B., *Experimental Methods in the Physical Sciences* **50**, 83 (2019).
8. Murzakhanov F., Latypova L., Mamin G., Sadovnikova M., von Bardeleben H., Gafurov M., *Magnetic Resonance in Solids* **26**, 24208 (2024).
9. MacKenzie K. J., Smith M. E., *Multinuclear solid-state nuclear magnetic resonance of inorganic materials*, Vol. 6 (Elsevier, 2002) p. 23–108.
10. Gracheva I. N., Murzakhanov F. F., Mamin G. V., Sadovnikova M. A., Gabbasov B. F., Mokhov E. N., Gafurov M. R., *Journal of Physical Chemistry C* **127**, 3634 (2023).

Influence of ^{14}N hyperfine interaction ...

11. Murzakhanov F. F., Mamin G. V., Orlinskii S. B., Gerstmann U., Schmidt W. G., Biktagirov T., Aharonovich I., Gottscholl A., Sperlich A., Dyakonov V., Soltamov V. A., *Nano Letters* **22**, 2718 (2022).